Structural and entropic modes in supercooled liquids: experimental and theoretical investigation



2003 J. Phys.: Condens. Matter 15 S1181

(http://iopscience.iop.org/0953-8984/15/11/337)

INSTITUTE OF PHYSICS PUBLISHING JOURNAL OF PHYSICS: CONDENSED MATTER

J. Phys.: Condens. Matter **15** (2003) S1181–S1192 PII: S0953-8984(03)58344-8

# Structural and entropic modes in supercooled liquids: experimental and theoretical investigation

**R Di Leonardo[1], A Taschin[2,3], R Torre[2,3], M Sampoli[3,4] and G Ruocco[1]**

[1] Dipartimento di Fisica and INFM, Università di Roma 'La Sapienza', I-00185, Roma, Italy
[2] Dipartimento di Fisica, LENS and INFM, Università di Firenze, I-50019 Sesto, Firenze, Italy
[3] INFM, Unitá di Firenze, I-50019 Sesto, Firenze, Italy
[4] Dipartimento di Energetica, Università di Firenze, via S Marta, I-50139, Firenze, Italy

Received 3 December 2002
Published 10 March 2003
Online at stacks.iop.org/JPhysCM/15/S1181

**Abstract**

We studied the relaxation processes of glycerol by a transient grating experiment with polarization selectivity and optical heterodyne detection. The density response of supercooled glycerol, for a wavevector $q = 0.63\ \mu\text{m}^{-1}$, has been studied in that temperature range ($T = 200$–$340$ K), where the rearrangement of the structure ($\alpha$-relaxation) and thermal diffusion occur on the same timescale. A strong interaction between the two modes is observed, manifesting in a dip in the $T$ dependence of the apparent thermal conductivity and in a flattening of the apparent $\alpha$-relaxation time upon cooling. A parameter-free thermo-hydrodynamic model for the long-time response is developed. The model is capable of quantitatively reproducing the data and of explaining the observed phenomenology.

## 1. Introduction

Whenever an inhomogeneous temperature or pressure field exists inside a substance, heat and momentum will flow, giving rise to processes, thermal diffusion and sound propagation, which drive the system toward homogeneity. At low enough wavevector $q$ (i.e. at the typical $q$ values of a light scattering experiment) the timescales of the two processes are well separated, so that sound propagation is adiabatic and thermal diffusion isobaric. Every other microscopic dynamical process evolves on such a fast timescale that it enters the dynamic equations simply by determining the actual values of thermodynamic derivatives and transport coefficients. The situation changes when a liquid is supercooled below its melting temperature and the structural relaxation time, $\tau_\alpha$, rapidly grows upon cooling. When $\tau_\alpha$ becomes of the order of a sound-wave period we observe phenomena such as the sound-velocity dispersion and sound absorption which have been widely investigated by ultrasonic and Brillouin spectroscopy and commonly described in terms of a relaxing bulk modulus or viscosity [1, 2]. Upon further cooling, $\tau_\alpha$ reaches the timescale of the thermal diffusion, giving rise to a non-trivial diffusive heat equation, usually described in terms of specific-heat relaxation, and experimentally observed by specific

  

heat spectroscopy [3] and forced Rayleigh scattering [4, 5]. However, though both viscosity and specific heat relaxations are manifestations of the same microscopic process, there is no commonly accepted form for the equations governing the fluid dynamics in the region where structural relaxation and thermal diffusion occur on the same timescale. The main difficulty arises when more than one single thermodynamic derivative has to be generalized to have a frequency dependence and one has to introduce free parameters relating the relaxation times and shape parameters appearing in the various relaxation functions. In this paper, we present an optical heterodyne transient grating (HD-TG) experiment [6] of liquid and supercooled glycerol covering a wide temperature range. First we studied the material response, performing HD-TG experiments with selective polarization configurations, so that we proved in this glass-former the response is dominated by the density relaxation excited by thermal effects (also called impulsive stimulated thermal scattering, ISTS [7]). In the region where the structural and entropic modes are temporally overlapped, a strong interaction between the two modes is observed, manifesting as an apparent freezing of the structural relaxation time upon cooling, and a marked non-exponential decay of a long-time ISTS signal, usually governed by thermal diffusion. This interaction produces a dip in the $T$ dependence of the apparent thermal conductivity of different supercooled liquids [4–6] that were previously unexplained. The proposed model is thus capable of explaining these phenomena as the non-exponential decay of the long-time part of the ISTS data, providing the correct temperature behaviour of the thermal conductivity and structural relaxation times. ISTS data are quantitatively reproduced by a thermo-hydrodynamic model which assumes local thermodynamic equilibrium in an extended parameter space. Every parameter entering the model is a well defined physical quantity. Using literature data we are able to predict ISTS responses in very good agreement with the measured ones.

## 2. Transient grating experiments

In a transient grating (TG) experiment two high power laser pulses, obtained by dividing a single pulsed laser beam, interfere inside the sample and they produce a spatially periodic variation of the index of refraction, see figure 1. A second laser beam, typically of a different wavelength, is acting as a probe. It impinges on the induced grating at the Bragg angle and it produces a diffracted beam, spatially separated by the pump pulses and probe beam itself. This diffracted beam is the signal measured in a TG experiment and it yields dynamic information from the relaxing grating. This induced variation of the dielectric constant of the sample can be described by the following expression [8, 9]:

$$\Delta\varepsilon_{ij}(\boldsymbol{r},t) = \int \mathrm{d}\boldsymbol{r}' \int \mathrm{d}t'\, R^{\varepsilon}_{ijkl}(\boldsymbol{r}-\boldsymbol{r}', t-t') F^{ex}_{kl}(\boldsymbol{r}', t') \tag{1}$$

where $F^{ex}_{kl}$ represents the exciting force produced by the two pumping pulses of the pump, $k$ and $l$ being the Cartesian coordinates of the electric fields of these beams, while $j$ and $i$ refer to the electric fields of the probe and the diffracted beams, respectively. $R^{\varepsilon}_{ijkl}$ is the response function of the system that defines the dynamical properties of the experimental observable, the local dielectric tensor, $\Delta\varepsilon_{ij}$. The response function has a tensorial nature, $R_{ijkl}$, where the different components are selected through the excitation, probing and detection directions of polarizations. In the experiments performed here, the directions of the four electric fields were such that $i = j$ and $k = l$, so that only the $R_{\alpha\alpha\beta\beta}$ components were detected. We will consider $\alpha$ or $\beta = V$ if the polarization is orthogonal to the scattering plane, or $\alpha, \beta = H$ if the polarization is parallel to the scattering plane, see figure 1. The exciting force is defined by the interference field, $\boldsymbol{E}^{ex}(\boldsymbol{r}, t)$, produced by the two pumping beams, $\boldsymbol{E}^{ex}_1(\boldsymbol{r}, t)$

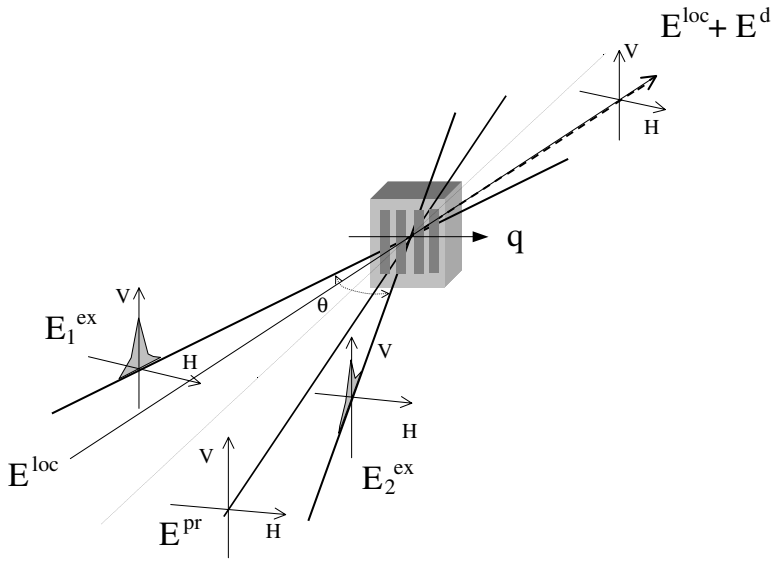


**Figure 1.** Sketch of the optical set-up used in a TG experiment with different polarization selections. $E^{ex}$ are the excitation laser pulses and the $E^{pr}$ and $E^{d}$ are the probing and diffracted beams, respectively. For each beam the possible polarization directions are reported. The local field ($E^{loc}$), used for the optical heterodyne detection, has a polarization parallel to the measured $E^{d}$ polarization.

and $\boldsymbol{E}_2^{ex}(\boldsymbol{r},t)$, according to the following equations: $F_{kl}^{ex}(\boldsymbol{r},t) = E_k^{ex}(\boldsymbol{r},t)E_l^{ex}(\boldsymbol{r},t)$, being $\boldsymbol{E}^{ex}(\boldsymbol{r},t) = \boldsymbol{E}_1^{ex}(\boldsymbol{r},t) + \boldsymbol{E}_2^{ex}(\boldsymbol{r},t)$. In the following calculations we will take the two pumping beams as plane waves with vertical polarization, $k = l = V$, and different wavevectors, $\boldsymbol{q}_1$ and $\boldsymbol{q}_2$, respectively, so that $\boldsymbol{E}_n^{ex}(\boldsymbol{r},t) = E_V^{ex}(\boldsymbol{q}_n,t) = \mathcal{E}_V^{ex}(t)\mathrm{e}^{\mathrm{i}(\boldsymbol{q}_n\cdot\boldsymbol{r}-\omega t)} + \text{c.c.}$ Considering the experimental geometry reported in figure 1 and assuming the impulsive limit in time (i.e. the excitation time is much shorter than the observable characteristic times) and in wavevector (i.e. the excitation spot size is much larger than the material wavelength scale), the expression of the excitation force can be easily calculated [8, 9]:

$$F_{VV}^{ex}(\boldsymbol{r},t) \propto (\mathcal{E}_V^{ex})^2\delta(t)[1+\cos(\boldsymbol{q}\cdot\boldsymbol{r})] \tag{2}$$

where $\boldsymbol{q} = \boldsymbol{q}_1 - \boldsymbol{q}_2$ and

$$|\boldsymbol{q}| = \frac{4\pi\sin(\theta_e/2)}{\lambda_e} \tag{3}$$

$\lambda_e$ and $\theta_e$ are the wavelength and the incidence angle of the excitation laser pulses. This wavevector defines the spatial modulation of the induced TG and hence the direction of diffraction of the probe field according to the phase-matching or Bragg condition: $\boldsymbol{q}_d = \boldsymbol{q}_{pr} + \boldsymbol{q}$, where $\boldsymbol{q}_{pr}$ and $\boldsymbol{q}_d$ are the wavevectors of the probe and diffracted field, respectively. The $r$-independent term of the excitation force does not contribute to the signal detected at the Bragg angle in the present experimental configuration. If, besides the approximations used above for the pumping beams, we consider the probe spot size to be much larger than the grating spacing and the frequency difference between the probe and diffracted beam and the propagation times through the sample to be negligible, the diffracted field in the $\boldsymbol{q}_d$ direction can be written as [8, 9]: $E_\alpha^d(\boldsymbol{r},t) \simeq \mathrm{e}^{\mathrm{i}(\omega t - \boldsymbol{q}_d\cdot\boldsymbol{r})}\Delta\varepsilon_{\alpha\alpha}(\boldsymbol{q},t)\mathcal{E}_\alpha^{pr} + \text{c.c.}$, where the probe is a continuous field with $\alpha$ polarization. Furthermore, considering equations (1) and (2) we easily find that $\Delta\varepsilon_{\alpha\alpha}(\boldsymbol{q},t) = R_{\alpha\alpha VV}^{\varepsilon}(\boldsymbol{q},t)(\mathcal{E}_V^{ex})^2$, that together with the previous equation defines completely

the diffracted field as $E^d_\alpha(\boldsymbol{r}, t) \simeq \mathrm{e}^{\mathrm{i}(\omega t - \boldsymbol{q}_d \cdot \boldsymbol{r})} R^\varepsilon_{\alpha\alpha VV}(\boldsymbol{q}, t)\mathcal{E}^{pr}_\alpha(\mathcal{E}^{ex}_V)^2$+c.c. In a HD-TG experiment [6] the measured signal is $S(t) \propto \langle(E^d + E^{loc})^2\rangle = \langle(E^d)^2\rangle + \langle(E^{loc})^2\rangle + 2\langle(E^d E^{loc})\rangle$, where $E^{loc}$ is the local field used as the beating field and $\langle\cdot\rangle$ represents the time average over the optical period. In the previous equation, the last term is the heterodyne contribution and it can be experimentally extracted by performing measurements characterized by selected phases of the local field. Finally, the heterodyne signal is

$$S^{HD}_{\alpha\alpha VV}(\boldsymbol{q}, t) \simeq R^\varepsilon_{\alpha\alpha VV}(\boldsymbol{q}, t)\mathcal{E}^{loc}_\alpha \mathcal{E}^{pr}_\alpha(\mathcal{E}^{ex}_V)^2. \tag{4}$$

Hence, according to the present experimental configuration and approximations, the HD-TG signal measures directly the relaxation processes defined by the tensor components $R^\varepsilon_{\alpha\alpha VV}$ of the dielectric response function. In particular, the two components $R^\varepsilon_{VVVV}$ and $R^\varepsilon_{HHVV}$ can be measured using the $\alpha = V$ or $H$ polarizations of the probe and diffracted fields. Formally, the dielectric response function contains all the physical information that these experiments can obtain. Nevertheless to define properly the connection between the material modes and the measured signal, we have to consider again the key processes of these experiments. Three steps can be identified: the first step is concerned with the forcing process and how effective it is in the excitation of the material modes; the second step defines how these modes propagate and modify the local dielectric properties of the material; the last step is the probing process that defines how the experiment measures the induced modification of the dielectric function. In the excitation process, the interference electric field interacts with the material through different physical mechanisms. As reported in [6, 10–12], three main effects have to be considered for near-infrared pulsed excitation in weakly absorbing materials (absorption typically due to overtone and/or combination of vibrational bands):

(a) heat deposition (this has been reported as thermal effects),
(b) the electrostriction effect (often called the Brillouin effect), and
(c) the electric torque applied to the molecules by the electric field because of the presence of an anisotropic polarizability (reported as the optical Kerr effect [13]).

Indeed electronic effects are also present but we will not take these into account since in the present experiment they do not contribute to the response function (in fact, they relax on a timescale much shorter than the pulse duration). So $F^{ex}$, that is the dielectric excitation force, indeed produces three excitation forces that drive the material modes: $F^{hd}$, a heat deposition force that drives directly the energy equation, $F^{es}$ an electrostrictive force that drives the density and $F^{et}$ a electrotorque force that drives the local orientational distribution of the molecules. All of these forces are normally present but, depending on the nature of the radiation–material interaction, some of them cannot be effective. The excitation brings the material out of equilibrium and, in the framework of non-linear response theory, the response function describes how the system relaxes back toward the equilibrium state. $R^\varepsilon$ describes the relaxation of the dielectric properties but, of course, it is directly connected with the relaxation functions of the material modes [6, 14]; which modes are effective in defining the dielectric relaxation depends on which forcing component is active and on the equations governing the modes' dynamics. In other words, since the equations that define the dynamics of thermal, density and orientational variables are coupled, more then one material mode has to be taken into account, even if a single force is efficient. For example, it has been shown by Taschin *et al* [10, 15] that in the glass-former *m*-toluidine the heating effect is the main driving force but, due to roto-translational coupling effects, both density and local orientation variables are present in the relaxation process. In this material, the heating force produces a density grating (or, better, a phase grating) and an orientational grating (a birefringence grating) and both these gratings will contribute to the probing process. Indeed, which excitation forces and material

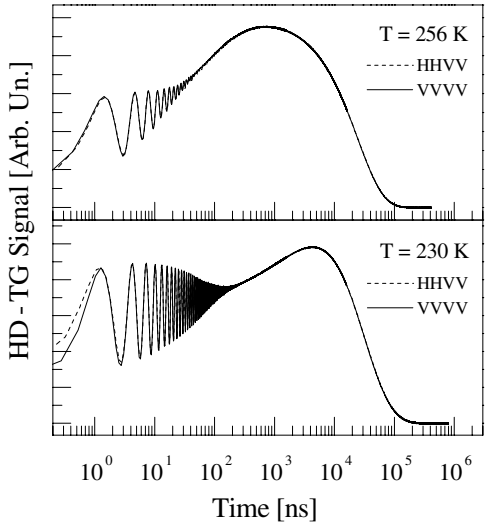


**Figure 2.** The measured signals, with optical heterodyne detection, corresponding to different polarization configurations are reported. The $S_{VVVV}$ and $S_{HHVV}$ signals in glycerol, obtained by the corresponding two polarization configurations, are identical, showing that no birefringence contribution is present.

modes are active has to be inferred by the experimental results. In fact, by performing HD-TG experiments characterized by different combinations of polarization it is possible to get a good insight into the excitation and relaxation processes [10, 11, 15]. So, if $S^{HD}_{VVVV} = S^{HD}_{VVHH}$ (hence $R^{\varepsilon}_{VVVV} = R^{\varepsilon}_{VVHH}$) this implies that the direction of field polarization in the excitation process is not relevant, and therefore the $F^{tq}$ force is not effective. If we compare $S^{HD}_{VVVV}$ with $S^{HD}_{HHVV}$, we can get information on which mode is active. $S^{HD}_{VVVV} = S^{HD}_{HHVV}$ shows that there are no polarization effects in the probing process, so no birefringence effects are present, and therefore no orientational response is present. Vice versa, if $S^{HD}_{VVVV} \neq S^{HD}_{HHVV}$, this implies that the orientational dynamics are active whatever the excitation is (direct due to the $F^{et}$ force or indirect due to the roto-translational coupling). In all the materials we studied (salol [11, 16], *m*-toluidine [10], *o*-terphenyl [6] and glycerol [17]), we found $S^{HD}_{VVVV} = S^{HD}_{VVHH}$. This suggests that the $F^{et}$ force is weak even in molecules characterized by a strongly anisotropic polarizability. Furthermore, in salol and *m*-toluidine, we found $S^{HD}_{VVVV} \neq S^{HD}_{HHVV}$ and vice versa in *o*-terphenyl and glycerol, where we found $S^{HD}_{VVVV} = S^{HD}_{HHVV}$. Summarizing, in glycerol (which has been investigated in the present work) we found $S^{HD}_{VVVV} = S^{HD}_{HHVV}$, see figure 2, that proves the absence of polarization effects in this material. This implies that the glycerol response is not affected by birefringence contributions and hence a study of mode dynamics can neglect the orientational variable, concentrating on the pure density response. Furthermore, in agreement with previous studies [18], we found also that the $F^{es}$ force is not active so that the whole measured response to be addressed is the density relaxation excited by thermal effects (such a TG experiment has also been called impulsive stimulated thermal scattering, or ISTS [7]).

## 3. Experimental details and results

The optical set-up and laser system has previously been described in [6]; here, we want to recall only the main features. In the present HD-TG experiment, two infrared ($\lambda_e = 1064$ nm) short

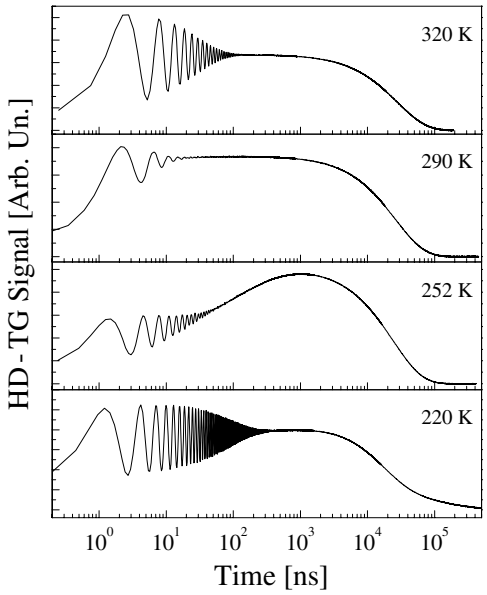


**Figure 3.** HD-TG data with $q = 0.63\ \mu\mathrm{m}^{-1}$ for the $VVVV$ configuration at four different temperatures. These spectra show clearly the acoustic, structural and thermal relaxation processes.

(100 ps) laser pulses cross each other in the sample volume at an angle of $\sim 6^\circ$ ($q = 0.63\ \mu\mathrm{m}^{-1}$) and their interference produces an impulsive, spatially modulated, heating due to absorption by an overtone of the OH stretching mode. The amplitude of the resulting density grating is probed by a third continuous wave (CW) laser beam ($\lambda_{pr} = 532$ nm) impinging on the induced grating at the Bragg angle. The diffracted beam is beaten with the local field, $E^{loc}$, and then it is stored as a function of time by a transient recorder and averaged over many thousands of pump pulses. The two excitations, the probe and the local fields, are obtained by dividing the pulsed and CW laser beams by a phase grating mask [6].

The $S^{HD}_{VVVV}$ data (corresponding to the vertical polarization for excitation pulses, probe and detection) were collected in the temperature range $T = 200$–$340$ K. Signals as long as 1.6 ms were recorded with a time resolution of 0.25 ns. Glycerol (99.5, Fluka) was transferred under a nitrogen atmosphere into a Teflon-coated cell with movable windows to reduce sample stress and cracking [19]. The cell was mounted on the cold finger of a cryostat and fitted with resistive heaters. A Pt100 thermometer is immersed in the sample, and the temperature is kept stable to within 0.1 K. In figure 3 we report four typical sets of ISTS data. They show, at all temperatures, damped acoustic oscillations at short times and thermal diffusion at long times. On decreasing the temperature, the structural relaxation mode appears at first as a strong acoustic damping, then later as a gradual rise of the ISTS signal, and at very low temperatures, because of coupling with the thermal mode, as a non-exponential decay of the long-time data. In the present paper, we focus on the long-time part of the ISTS signal ($t > 0.1\ \mu$s) where the acoustic transient is over and structural and entropy modes evolve isobarically. Selected ISTS data are reported in figure 4 showing two time regions: 'short times' ($t < 10\ \mu$s) in the inserts and longer times in the main panels. It can be noted that at short times the amplitude of the density grating (ISTS signal) increases with a stretched exponential law, due to structural relaxation. On lowering the temperature, the characteristic

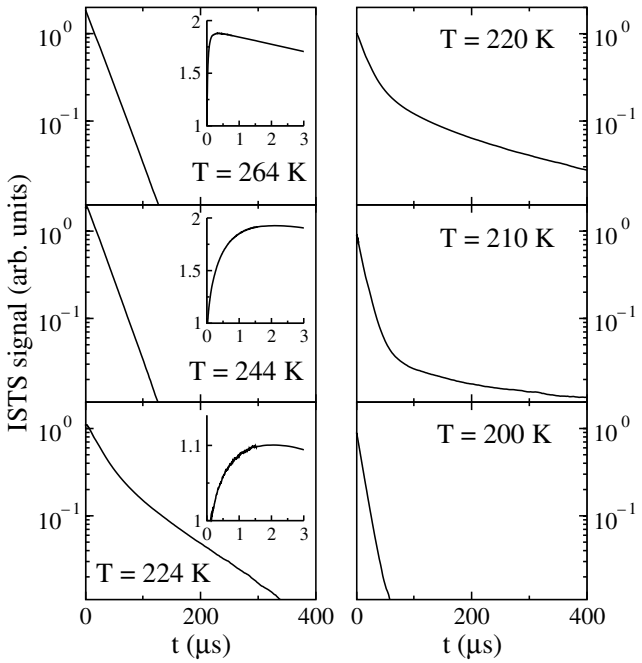


**Figure 4.** ISTS data of supercooled glycerol at selected temperatures are reported in logarithmic scale and normalized to unity at about $t = 0.1$ $\mu$s. The inserts show a blow up of the short-time region, where the structural relaxation gives rise to a rising signal.

time of this rising component stops growing while its intensity (the amplitude of the stimulated density grating associated with the structural relaxation) vanishes. At longer times the heat diffuses and the density grating decays to zero. This long-time decay, which in the absence of coupling is exponential (due to the diffusive character of the heat equation) [14], now splits into two components. The faster component is nearly exponential and its time constant goes through a maximum and gives rise to a dip in the apparent thermal diffusivity, as already reported for OTP in [6]. The slower component shows strong non-exponentiality. It flattens out and its intensity disappears as the temperature is lowered. To be more quantitative, we fitted the data with two stretched exponentials for the 'structural' rising component and the long-time tail, and a simple exponential for the intermediate-time component (apparent thermal diffusion). The decay rates of the short and intermediate components are reported in figure 5; we note that, in order to characterize the rate of the stretched exponential ($\exp[-(\gamma t)^{\beta}]$), we used the inverse average time $\langle\tau\rangle^{-1} = \gamma\beta/\Gamma(1/\beta)$, where $\Gamma$ is the Euler gamma function. At high temperatures, the structural relaxation decay rate (○) is described by a Vogel–Tamman–Fulcher (VTF) law (full curve). The parameters $B = 2260$ K, $T_{VTF} = 131$ K of VTF law, $\gamma_{VTF} = \tau_0^{-1}\exp[-B/(T - T_{VTF})]$ are taken from dielectric spectroscopy [20] while $\tau_0 = 1.4 \times 10^{-15}$ s is scaled to fit the data. At temperatures lower than ∼240 K the short-time increasing component ceases to represent the structural relaxation and flattens at around a value of 4 $\mu$s. At about the same temperature, the apparent thermal decay rate deviates from the expected smooth behaviour (see the insert of figure 5) and exhibits a dip at $T \approx 230$ K. The overall scenario depicted in figure 5 suggests the existence of an interaction between the structural and thermal relaxation dynamics that leads to a complex relaxation-time pattern.

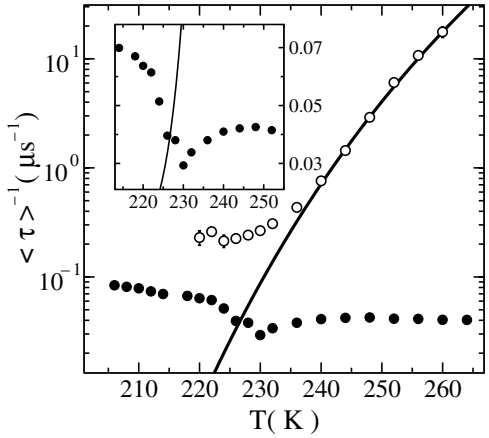


**Figure 5.** Temperature dependence of characteristic rates for the short rising component-apparent structural relaxation (○) and intermediate exponential decay-apparent thermal diffusion (●). The full curve is the VTF law $\gamma_{VTF} = \tau_0^{-1} \exp[-2260\ \mathrm{K}/(T - 131\ \mathrm{K})]$.

## 4. Non-equilibrium thermodynamic model and data interpretation

In the following, we will introduce a non-equilibrium-thermodynamic (NET) model that will allow us to compute the temperature evolution of this relaxation-time pattern and we find very good agreement with the experimental observations. NET [21] provides a very powerful framework to study irreversible processes, such as heat conduction, diffusion and viscous flow, from a unified point of view. However, in this formalism, it is not straightforward to consider the non-exponentiality observed in the structural relaxation dynamics. On the contrary, the presence of a large number of internal relaxing variables can be easily taken into account, provided that local thermodynamic equilibrium is valid in the extended parameter space. Therefore, following Allain *et al* [4], we choose to represent the observed non-exponentiality as the result of the superposition of $N$ linearly relaxing variables. The number $N$ should not be read as a number of well-defined physical variables, but rather as the discrete representation of either a distribution of independent Debye relaxing variables, or a single strongly non-exponential relaxing variable. The choice of representing a distribution of relaxation times as a sum of exponential decays is imposed by our will to approach the problem within the framework of non-equilibrium thermodynamics in its usual linear formulation. It is important to note that the specific studies and experiments presented in this work do not allow one to find whether the underlying relaxation process is homogeneous and intrinsically non-exponential or if it is heterogeneous, i.e. the superposition of different, spatially separated, genuine Debye processes (see [22] for a comprehensive review on the subject). In this hypothesis, the Gibbs free energy law per unit mass is

$$\mathrm{d}g = v\,\mathrm{d}p - s\,\mathrm{d}T - \sum_{i=1}^{N} A^i\,\mathrm{d}\xi^i \tag{5}$$

where $p$ is the pressure, $s$ is the entropy, $A^i$ is the affinity of the $i$th relaxation process and $\xi^i$ is the corresponding progress variable (or order parameter). We remark that the following analysis is independent from the precise physical meaning of the $\xi$ parameters; it only relies on the fact that

(i) they are frozen on a timescale shorter than the structural relaxation time ($\tau_\alpha$);
(ii) they relax toward their equilibrium values on a timescale much greater than $\tau_\alpha$.

As noted above, we are interested in the time region where the pressure becomes and stays uniform. In this time region, the linearized non-equilibrium thermodynamic equations [21] written in terms of the $q$ components of the thermodynamic variables (e.g. $T$ stands for $T(t) = \int \exp(\mathrm{i}\boldsymbol{qr})T(,t)$), are

$$\begin{aligned} &p = 0 \\ &T_0\rho_0(\partial s/\partial t) = -q^2\lambda T \\ &\partial\xi^i/\partial t = -\beta^i A^i \end{aligned} \tag{6}$$

where $T_0$ ($\rho_0$) is the average temperature (density), $\lambda$ is the thermal conductivity and $\beta^i$ are phenomenological constants. The first equation of (6) comes from the linearized combined mass momentum conservation laws:

$$\partial^2\rho/\partial t^2 + (\eta q^2/\rho_0)\partial\rho/\partial t + q^2 p = 0.$$

After acoustic transient, the terms involving derivatives of density are negligible. The second and third equations of (6) represent the energy conservation law and the phenomenological relations for the relaxation processes, respectively. In order to close the above set of equations, we use the local thermal equilibrium in the extended parameter space:

$$\begin{aligned} &\rho = \rho(p, T, \xi^1, \ldots, \xi^N), \\ &s = s(p, T, \xi^1, \ldots, \xi^N), \\ &A^i = A^i(p, T, \xi^i). \end{aligned} \tag{7}$$

For simplicity, we assume that the thermodynamic affinity $A^i$ does not depend on $\xi^j$ for $j \neq i$. Differentiating the above equations and substituting in (6) we obtain

$$\rho = -\rho_0\alpha^\infty T + (\rho_0^2 c_p^\infty/T_0)\sum_{i=1}^{N}\Delta^i(\xi_p^i/\xi_T^i)\zeta^i \tag{8}$$

$$\partial T/\partial t = -\Gamma_H^\infty T - \sum_{i=1}^{N}\Gamma_R^i\Delta^i(T - \zeta^i) \tag{9}$$

$$\partial\zeta^i/\partial t = -\Gamma_R^i(\zeta^i - T), \tag{10}$$

where we have introduced the following symbols:

$$\begin{aligned} &\alpha^\infty = -\rho^{-1}(\partial\rho/\partial T)_{p\xi} && c_p^\infty = T_0(\partial S/\partial T)_{p\xi} \\ &\Delta^i = T_0 A_\xi^i \xi_T^{i2}/c_p^\infty && A_\xi^i = (\partial A^i/\partial\xi^i)_{pT} \\ &\xi_p^i = (\partial\xi^i/\partial p)_{A^i T} && \xi_T^i = (\partial\xi^i/\partial T)_{A^i p} \\ &\zeta^i = \xi^i/\xi_T^i && \Gamma_H^\infty = \lambda q^2/\rho_0 c_p^\infty. \end{aligned} \tag{11}$$

The ISTS density response is obtained by solving (9), (10) for the initial condition $T(0) \neq 0$, $\xi^i(0) = 0$ and then substituting in (8). To reduce the number of parameters, we use the simplifying assumption that $\xi_p^i/\xi_T^i$ is independent of $i$ [4]. In that case, $\rho(t)$ can be written as

$$\rho(t)/\rho(0) = -T(t)/T(0) - \frac{\Delta\alpha}{\alpha^\infty}\frac{c_p^\infty}{\Delta c_p}\sum_{i=1}^{N}\Delta^i\zeta^i(t) \tag{12}$$

where $\Delta\alpha$ and $\Delta c_p$ are the jumps from the relaxed to the unrelaxed (with respect to the $\zeta^i$) values of the corresponding thermodynamic derivatives:

$$\begin{aligned} &\Delta\alpha = -\rho_0\sum A_\xi^i\xi_p^i\xi_T^i \\ &\Delta c_p = T_0\sum A_\xi^i(\xi_T^i)^2. \end{aligned}$$

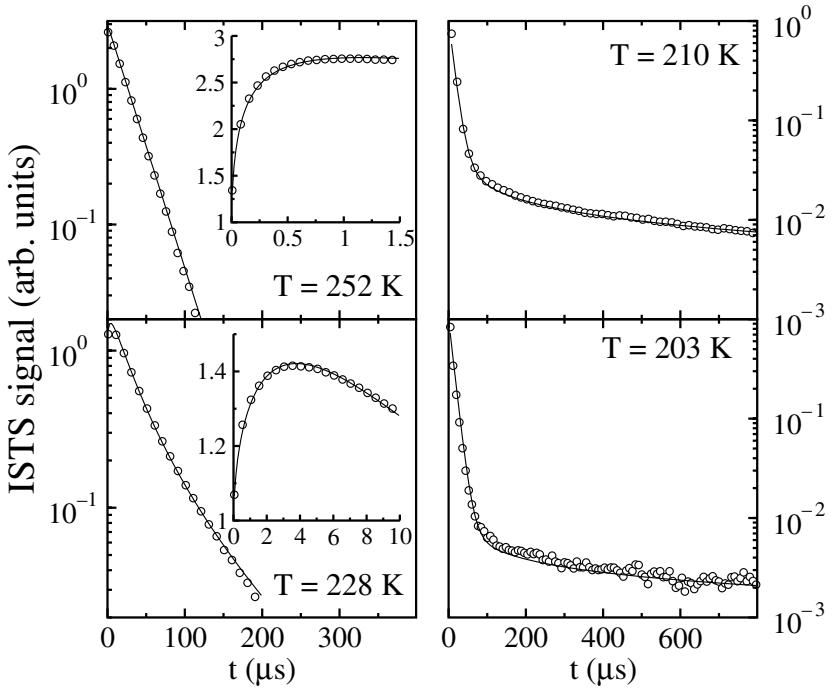


**Figure 6.** ISTS data (○) and the predicted signal (full curve) for four different temperatures. The agreement is very good through the whole structural-entropic coupling region.

It can easily be shown that in the limit $\Gamma_R^i \ll \Gamma_H^\infty$—i.e. at low-$T$ or high-$q$ values—this model predicts a density–density correlation function which at long times decays as

$$\phi_q(t) \propto \sum_{i=1}^{N} \Delta^i \exp[-\Gamma_R^i t]. \tag{13}$$

We know from photocorrelation experiments, mode coupling theory and molecular dynamics simulations that the above correlator is very well described by a stretched exponential $\exp[-(t/\tau_\alpha)^\beta]$, where $\beta$ slightly changes with temperature and $\tau_\alpha$ obeys a VTF law. Relying on this consideration, we arbitrarily choose a distribution of $N = 150$ logarithmically spaced rates $\Gamma_R^i = (\Gamma_\alpha)10^{x_i}$, $x_i = -1 + i/28$, with weights $\Delta^i$ such that the sum (13) reconstructs a stretched exponential with $\beta = 0.65$ [3, 18]. We note that, given the constraints in the model, the number of input parameters does not change with $N$. We also remark that, for large enough $N$ (>10), the solution is practically independent of $N$. This determines the weights, apart from a constant factor which in turn can be easily fixed by the value of $\Delta c_p/c_p^\infty = \sum \Delta^i$ from specific heat spectroscopy data [3]. The temperature simply changes the value of $\Gamma_\alpha$ which is assumed to obey the already quoted VTF law. We can assume $\Gamma_H^\infty(T) = (c_p^0/c_p^\infty)\Gamma_H^0(T)$, where $\Gamma_H^0(T)$ is the extrapolation to the whole temperature range of ISTS thermal decay rates at high temperature. Finally, from $\rho(T)$ data across the glass-transition temperature [23], one finds $\Delta\alpha \sim 3.2\alpha^\infty$. We are now left with no more free parameters: for each temperature we can compute the ISTS signal and compare it to the experimental data. As examples, the results of this comparison are shown in figure 6 for four different temperatures, showing an excellent agreement between the data (○) and the model (full curve) in the whole of the temperature range examined. A complementary and more insightful way of representing complex time

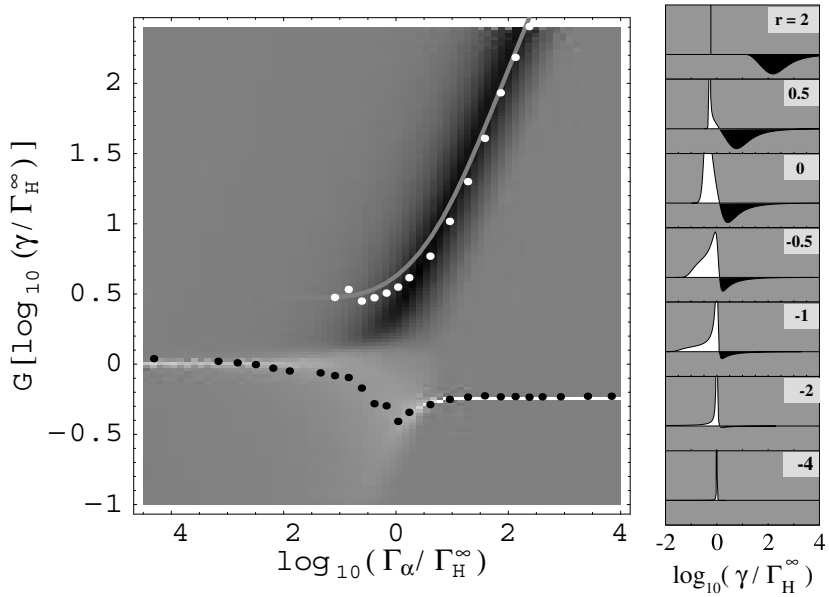


**Figure 7.** Computed evolution of the distribution of rates $G$ as a function of the logarithmic ratio $r = \log_{10}(\Gamma_\alpha/\Gamma_H^\infty)$ between the structural relaxation characteristic rate and the infinite frequency thermal decay rate. Circles in the left panel represent the experimental values.

responses consists in performing an inverse Laplace transform analysis:

$$I(t) = \int_{-\infty}^{\infty} G(\log\gamma)\exp[-\gamma t]\,\mathrm{d}\log\,\gamma. \tag{14}$$

In other words, one can think of the ISTS signal as a superposition of exponentials and ask how the weight function $G$ evolves across the coupling region. In this representation, it is easier to visualize the analysed phenomenology as the interaction between an exponential thermal process and a broad distribution of relaxing variables. As a consequence, the relation between the flattening in the 'structural' rate, the dip in the thermal rate and the appearance of a long-time tail becomes evident. Such an analysis has been carried out on the simulated signals and is summarized in figure 7. The top figure in the right panel represents $G$ in the high-temperature region where no coupling is present. Structural relaxation manifests itself as a rising (negative weight) stretched (broad distribution) exponential, while at longer times (smaller rates) thermal diffusion contributes to the signal with an exponentially (narrow) decaying (positive weight) component. As the temperature is lowered, the broad structural mode moves to shorter rates until the tail of its rate distribution reaches the entropy-mode timescale. As a result, the timescale of the negative component ceases to vary and its intensity vanishes. On the other hand, the positive component broadens, moving to smaller rates and then splits into two components: a narrow one which moves to larger rates, lowering the temperature, and a broad one which becomes flatter and flatter and decays to zero. In the left panel of figure 7, we report the evolution of $G$ as a function of $\log_{10}(\Gamma_\alpha/\Gamma_H^\infty)$. Black and white regions represent negative and positive weights, respectively. The circles represent the normalized average rates for the rising (white) and first part of the decaying (black) portion of the experimental ISTS signal. The full upper line is the computed inverse average time $1/\langle\tau\rangle$ of the negative component. In conclusion, a non-equilibrium thermodynamic model, based on

the assumption of local thermodynamic equilibrium in an extended parameter space, accounts for the rich phenomenology observed in the ISTS experiments. In particular, using new ISTS data on supercooled glycerol in the temperature region where the structural relaxation and the thermal diffusion process take place on the same timescale, we have demonstrated that the model is able to reproduce experimental data using data from other experiments in the literature. Further investigations into the possibility of assuming local thermodynamic equilibrium in supercooled liquids are crucial to the development of a thermodynamic description of glass-forming liquids.

## Acknowledgments

This work was supported by INFM, MIUR and EC grant no HPRI-CT1999-00111.

## References

[1] Mountain R D 1968 *Rev. Mod. Phys.* **38** 205
[2] Zwanzig R 1988 *J. Chem. Phys.* **88** 5831
[3] Birge N O 1986 *Phys. Rev.* B **34** 1631
[4] Allain C, Lallemand P and Ostrowsky N 1976 *Mol. Phys.* **31** 581
Allain C and Lallemand P 1979 *J. Physique* **48** 679
[5] Köhler W, Fytas G, Steffen W and Reinhardt L 1996 *J. Chem. Phys.* **104** 248
[6] Torre R, Taschin A and Sampoli M 2001 *Phys. Rev.* E **64** 61504
[7] Yang Y and Nelson K A 1995 *Phys. Rev. Lett.* **74** 4883
[8] Eichler H J, Gunter P and Pohl D W 1986 *Laser-Induced Dynamic Gratings* (Berlin: Springer)
[9] Yan Y and Nelson K A 1987 *J. Chem. Phys.* **87** 6240
Yan Y and Nelson K A 1987 *J. Chem. Phys.* **87** 6257
[10] Taschin A, Torre R, Ricci M, Sampoli M, Dreyfus C and Pick R M 2001 *Europhys. Lett.* **56** 407
[11] Glorieux C, Nelson K A, Hinze G and Fayer M D 2002 *J. Chem. Phys.* **116** 3384
[12] Hinze G, Francis R S and Fayer M D 1999 *J. Chem. Phys.* **88** 6477
[13] Torre R, Bartolini P and Pick R M 1998 *Phys. Rev.* E **57** 1912
Torre R, Bartolini P, Ricci M and Pick R M 2000 *Europhys. Lett.* **52** 324
[14] Yang Y and Nelson K A 1995 *J. Chem. Phys.* **103** 7722
Yang Y and Nelson K A 1995 *J. Chem. Phys.* **103** 7732
[15] Pick R M, Dreyfus C, Azzimani A, Taschin A, Ricci M, Torre R and Franosch T 2003 *J. Phys.: Condens. Matter* **15** S825
[16] Taschin A *et al* 2003 in preparation
[17] Di Leonardo R, Taschin A, Sampoli M, Torre R and Ruocco G 2003 *Phys. Rev.* E **67** 015102(R)
[18] Paolucci D M and Nelson K A 2000 *J. Chem. Phys.* **112** 6725
[19] Halalay I and Nelson K A 1990 *Rev. Sci. Instrum.* **61** 3623
[20] Lunkenheimer P *et al* 1995 *Europhys. Lett.* **33** 611
[21] de Groot S R and Mazur P 1962 *Non Equilibrium Thermodynamics* (New York: Dover)
[22] Richert R 2002 *J. Phys.: Condens. Matter* **14** R703
[23] Ubbelohde A R 1965 *Melting and Crystal Structure* (Oxford: Clarendon)
[24] Demoulin C, Montrose C J and Ostrowsky N 1974 *Phys. Rev.* A **9** 1740